Modeling of electric field in silicon micro-strip detectors irradiated with neutrons and pions

2014 JINST 9 P10016

(http://iopscience.iop.org/1748-0221/9/10/P10016)

PUBLISHED BY IOP PUBLISHING FOR SISSA MEDIALAB

RECEIVED: *April 7, 2014*
REVISED: *August 13, 2014*
ACCEPTED: *September 20, 2014*
PUBLISHED: *October 30, 2014*

Modeling of electric field in silicon micro-strip detectors irradiated with neutrons and pions[1]

G. Kramberger,[a,2] **V. Cindro,**[a] **I. Mandić,**[a] **M. Mikuž,**[a,b] **M. Milovanović**[a] **and M. Zavrtanik**[a]

[a] *Jožef Stefan Institute, Jamova 39, SI-1000 Ljubljana, Slovenia*
[b] *University of Ljubljana, Faculty of Mathematics and Physics, Jadranska 19, SI-1000 Ljubljana, Slovenia*

E-mail: Gregor.Kramberger@ijs.si

ABSTRACT: Edge-TCT method was used to extract velocity profiles in heavily irradiated silicon micro-strip detectors. Detectors were irradiated up to 10^{16} cm^{-2} with reactor neutrons, 200 MeV pions and a combination of both. A simple electric field model assuming two space charge regions at each side of the detector and neutral bulk in-between was found to describe the field profile. It was observed that after heavy irradiation a sizeable electric field is present in the entire detector volume. For pion-irradiated detectors strikingly different profiles were obtained and attributed to the large oxygen concentration in the detector bulk. The model parameters were also studied during the long term annealing. The space charge region near the strips was found to shrink which in turn leads to larger electric field and impact ionization. The model parameters extracted from the measurements were fed to the device simulation program which showed reasonable agreement between simulated and measured data at lower fluences.

KEYWORDS: Solid state detectors; Radiation damage evaluation methods; Radiation-hard detectors; Detector modelling and simulations II (electric fields, charge transport, multiplication and induction, pulse formation, electron emission, etc)

[1] Work performed in the framework of the CERN-RD50 collaboration.
[2] Corresponding author.

doi:10.1088/1748-0221/9/10/P10016

Contents

1 Introduction **1**

2 Experiment and samples **2**

3 Velocity profiles of neutron irradiated sample **3**

4 Field modeling in neutron irradiated detector **6**
- 4.1 Active region — junction side 7
- 4.2 Electric field at the back electrode 9
- 4.3 Neutral bulk 10

5 Pion and mixed irradiated detectors **10**

6 Long term annealing **12**

7 Simulation of the Edge-TCT measurements **14**

8 Conclusions **16**

2014 JINST 9 P10016

1 Introduction

The upgrade of the Large Hadron Collider (HL-LHC) [1] foreseen for the next decade represents a serious challenge for detectors. High rates of particles and consequent radiation damage [2], particularly in detector components close to the interaction region are posing new demands to the detector development. Position sensitive detectors in the innermost part will be exposed to fast hadron fluences up to $1.6 \cdot 10^{16}\,\mathrm{cm}^{-2}$ [3]. A decade ago the use of silicon detectors beyond 10^{15} of fast hadrons/cm^2 was seen as a major challenge [4]. As a result of extensive research it seems now that the combination of readout at segmented n^+ electrodes, high voltage operation, carefully planned annealing scenario and proper electrode design, both for planar and 3D detectors, leads to efficient operation of silicon detectors over the whole fluence range at the HL-LHC [5–8]. The underlying physics reason for this is the onset of impact ionization [9, 10], which causes charge multiplication close to the electrodes and thus improves charge collection well beyond the one predicted from extrapolation of measurements at lower fluences [11, 12] .

The knowledge of the electric field profile is important to predict and understand the operation of detectors. There were attempts to calculate the electric field in an irradiated detector from the energy levels measured with Deep Level Transient Spectroscopy or Thermally Stimulated Current techniques [13, 14], however none of them were able to reproduce the measured charge collection with proper trap parameters over the full fluence range.

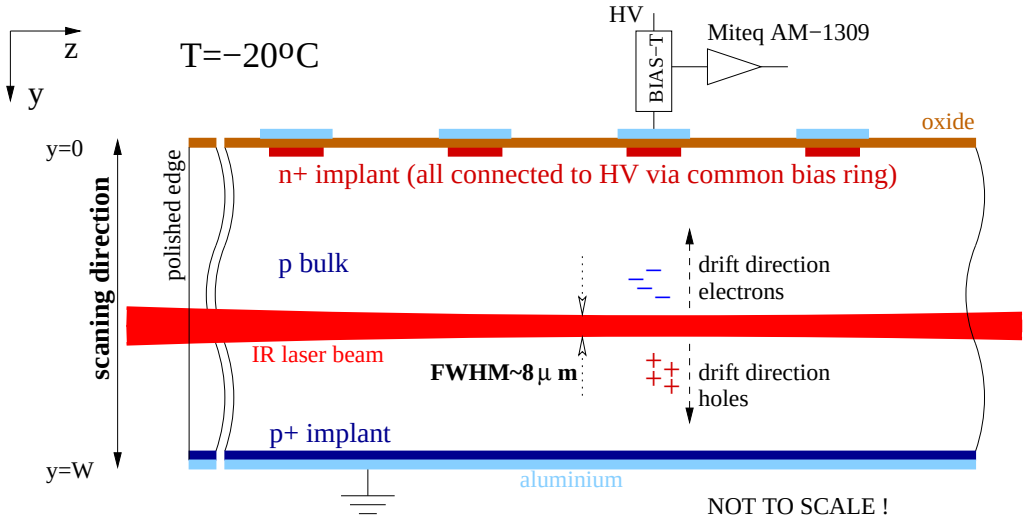

Figure 1. Schematic view of the Edge-TCT technique. Three neighbouring Al strips on each side of the readout Al strip were also connected to the same potential as implants.

The transient current technique (TCT) is a widely used tool for investigation of the electric field profile in semiconductor detectors [15]. The current induced in the readout electrodes after generation of free carriers by a light pulse is monitored by a fast current amplifier. The induced current is proportional to the velocity of charge carriers, hence the electric field profile can be extracted from its time evolution. At fluences in the HL-LHC range the trapping distance becomes so short [16–18] that it is impossible to probe the electric field in the detector bulk from the pulse shape, when charge carriers are generated close to the surface (top-TCT). However if the edge of the detector is illuminated with a focused IR laser beam — so called Edge-TCT [19] — the electric field can be probed also in the presence of high trapping. This technique was used in this work to establish the electric field profile in float zone n^+-on-p detectors at different fluences. Preliminary results of modeling, obtained after neutron irradiation [20], were finalized and extended with the analysis after pion and mixed irradiations and during long term annealing. Finally, parameters describing the electric field profiles were used to simulate the Edge-TCT measurements.

2 Experiment and samples

The basic principle of the Edge-TCT technique is shown in figure 1. A carefully polished edge of the detector is illuminated with a narrow laser beam of infrared light ($\lambda = 1064$ nm, ≈ 40 ps pulse width, 200 Hz repetition rate). Electron-hole pairs are created almost uniformly along the beam in a similar way as for minimum ionizing particles. The beam position, and by that the depth at which the carriers are generated, is controlled by moving stages with sub-micron precision. The carriers start to drift in the electric field and induce a signal, read out by the current amplifier (MITEQ AM-1309, 10 kHz–1 GHz) connected to one of the Al strips. An average of 400 pulses is recorded by a 1.5 GHz oscilloscope at each scan position. The detailed description of the setup and the measurement technique can be found in ref. [19].

2014 JINST 9 P10016

The measurements were done on three *p*-type micro-strip detectors processed by HPK[1] on float zone silicon. Initial resistivity of the silicon was around 5 kΩ cm, resulting in a full depletion voltage of $V_{\text{fd}} \approx 180$ V for 300±15 μm thick detectors. Detectors had 1 cm long AC coupled n^+ strips with a pitch of 100 μm and implant width of 20 μm.

3 Velocity profiles of neutron irradiated sample

One of the detectors was irradiated in steps with neutrons in the TRIGA nuclear reactor of the Jožef Stefan Institute in Ljubljana [21, 22] up to the 1 MeV neutron equivalent fluence of 10^{16} cm^{-2} (steps of $1,1,3,5 \cdot 10^{15}$ cm^2). The uncertainty in the fluence scale is estimated to be less than 10%. Between irradiation steps the detector was annealed up to the accumulated time of 80 min at 60°C (in steps of 10, 10, 20 and 40 min) — so called CERN scenario measurement. After each annealing step Edge-TCT measurements were performed at $T = -20$°C, while the measurement of a non-irradiated detector was done at $T = 20$°C. A Peltier element was used for heating and cooling, thus allowing the detector to remain mounted in the setup also during annealing.

An infrared laser beam pulse creates electron-hole pairs along its path at a given depth y (see figure 1). The induced current I at time t after the generation of electron-hole pairs at depth y in the detector is given by [19]

$$I(y,t) = I_e(y,t) + I_h(y,t) \approx e_0 \, N_{e-h} \, \frac{1}{W} \left[v_e(y_e(t)) \, e^{-t/\tau_{\text{eff},e}} + v_h(y_h(t)) \, e^{-t/\tau_{\text{eff},h}} \right], \tag{3.1}$$

where y denotes the beam position, e_0 elementary charge, N_{e-h} number of generated electron hole pairs and $v_{e,h}$ the drift velocities at a given $y_{e,h}(t)$ (see figure 1). Note that eq. (3.1) holds only approximately as carriers close to the strips are generated in a non-uniform electric field and therefore drift velocity terms in eq. (3.1) represent an average over the strip pitch at a given $y(t)$. The weighting field term is effectively $1/W$, where W denotes the detector thickness. This is a consequence of uniform charge generation underneath several adjacent strips [19].

Shortly after generation of non-equilibrium carriers trapping can be neglected $(\exp(-t/\tau_{\text{eff},e,h}) \approx 1)$ and the induced current can be written as

$$I(y, t \sim 0) \approx e_0 \, N_{e,h} \, \frac{v_e(y) + v_h(y)}{W}. \tag{3.2}$$

The induced current at $t \approx 0$ is therefore proportional to the sum of drift velocities at a given depth. But the initial rise of the measured current pulse, as for example observed in figure 2a, is limited by the transfer function of electronics, mostly by the sample capacitance and to lesser extent by the bandwidth of the amplifier, bias-T and oscilloscope, which all result in typical peaking times of around $\tau_{\text{peak}} \leq 1$ ns. The value of the measured current for $t < \tau_{\text{peak}}$ can however be exploited to estimate the induced current shortly after the generation of free carriers. In fact, this value reflects a weighted average of the velocity sum across the vicinity of y in eq. (3.1). The value of $\tau_{\text{sample}} = 600$ ps was found as a good compromise and was used in the rest of the paper. Values obtained with shorter intervals are less affected by spatial smearing and trapping effects at high fluences, but lead to larger fluctuations in the velocity profile.

[1] Hamamatsu Photonics, Japan.

2014 JINST 9 P10016

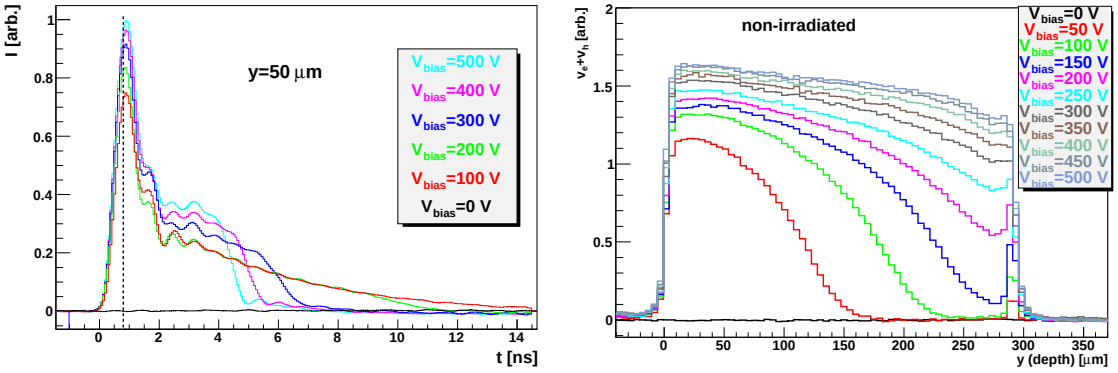

(a) (b)

Figure 2. (a) Measured current pulses in a non-irradiated detector after generation of free carriers at $y = 50$ μm and $T = 20°$C. The initial part up to $\sim$ 2ns is due to drift of electrons and holes and the long tail due to drift of holes only. The dashed vertical line denotes τ_{sample} used for determining the velocity profile. (b) Velocity profiles measured at different bias voltages (finalized from [20]).

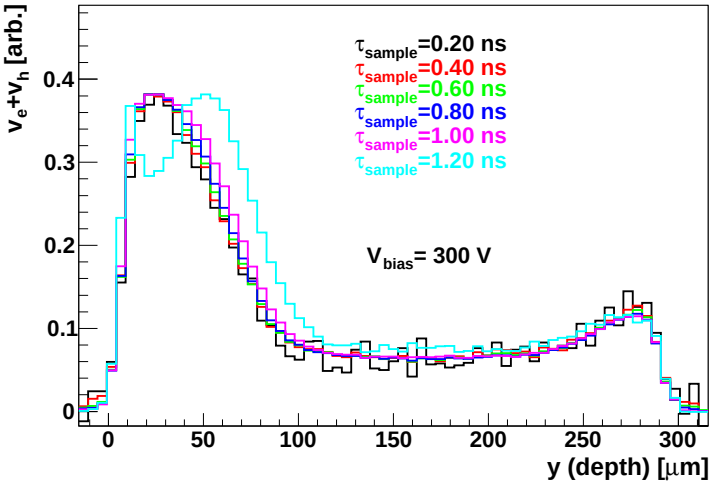

Figure 3. Dependence of velocity profile on the interval $[0, \tau_{\text{sample}}]$ for a detector irradiated to $\Phi_{\text{eq}} = 5 \cdot 10^{15}$ cm^{-2}, annealed for 80 min and biased to 300 V. All plots are normalized to $\tau_{\text{sample}} = 200$ ps.

An example of measured current pulses at $y = 50$ μm for different bias voltages in an non-irradiated detector is given in figure 2a. A scan across the detector depth was made to produce the velocity profile in the detector. For a non-irradiated detector (figure 2b.) it can be clearly seen that the velocity of charges injected in non-depleted bulk vanishes. The difference in doping at the p^+ contact (back side of the detector) results in appearance of electric field at the back even at voltages below $V_{\text{fd}} \sim 180$ V. At $V > V_{\text{fd}}$ the velocity starts to saturate and there is little difference between profiles at 300 V and 500 V.

At very high fluences the effective trapping times become comparable with τ_{sample} and consequently the choice of τ_{sample} could influence the extracted velocity profiles. Analysis with different τ_{sample} were done for a heavily irradiated detector and yielded comparable drift velocity profiles up to $\tau_{\text{sample}} = 1$ ns as demonstrated in figure 3.

2014 JINST 9 P10016

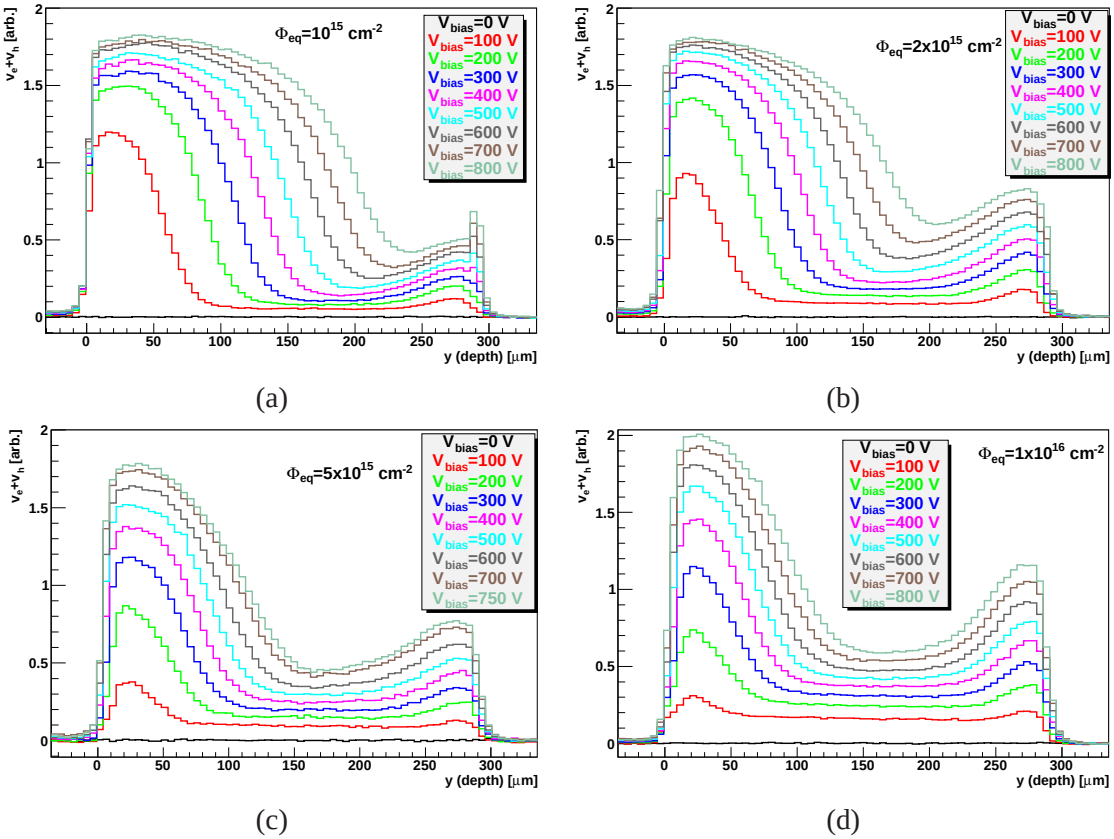

Figure 4. Velocity profiles at different bias voltages for irradiated detector at different fluence steps: (a) $1 \cdot 10^{15}\,\mathrm{cm}^{-2}$, (b) $2 \cdot 10^{15}\,\mathrm{cm}^{-2}$, (c) $5 \cdot 10^{15}\,\mathrm{cm}^{-2}$ and (d) $1 \cdot 10^{16}\,\mathrm{cm}^{-2}$. The profiles were measured after 80 min annealing at each irradiation fraction (finalized from [20]).

Effective trapping times extrapolated from the measurements in p-type detectors at lower fluences are around 500 ps [18] for electrons and holes at $\Phi_{\mathrm{eq}} = 5 \cdot 10^{15}\,\mathrm{cm}^2$. Although τ_{sample} is comparable to the extrapolated effective trapping times it seems that choice of a shorter time interval does not change the measured velocity profile significantly. This indicates that for $t < 600$ ps the response of the amplifier is mainly due to the motion of the carriers on time scale substantially shorter than the effective trapping times at this fluence.

The velocity profiles of a detector, irradiated with neutrons to different fluences are shown in figure 4. For high bias voltages the velocity appears almost saturated at the strip side for all fluences, except the highest. For all the profiles the same detector and laser setting were used so that the velocity profiles for different fluences can be compared to within $\approx 10\%$. A slightly lower value of saturated velocity for the non-irradiated detector (see figure 2b) can be attributed to the larger $T = 20^{\circ}\mathrm{C}$ and consequently larger absorption of light in non-active part of the sensor in front of the strips as well as reduced mobility at the higher temperature. Velocity profiles close to the strips, however, exhibit a non-negligible increase at highest voltages for $\Phi_{\mathrm{eq}} = 10^{16}\,\mathrm{cm}^{-2}$, which can be attributed to charge multiplication; i.e. increase of N_{e-h} in eq. (3.2). The lower value at intermediate voltages as compared to lower fluences is a consequence of trapping.

It is important to observe that the drift velocity increases also at the back. Such a profile is known as “double peak electric field profile” [14], but it is for the first time that it is observed at

2014 JINST 9 P10016

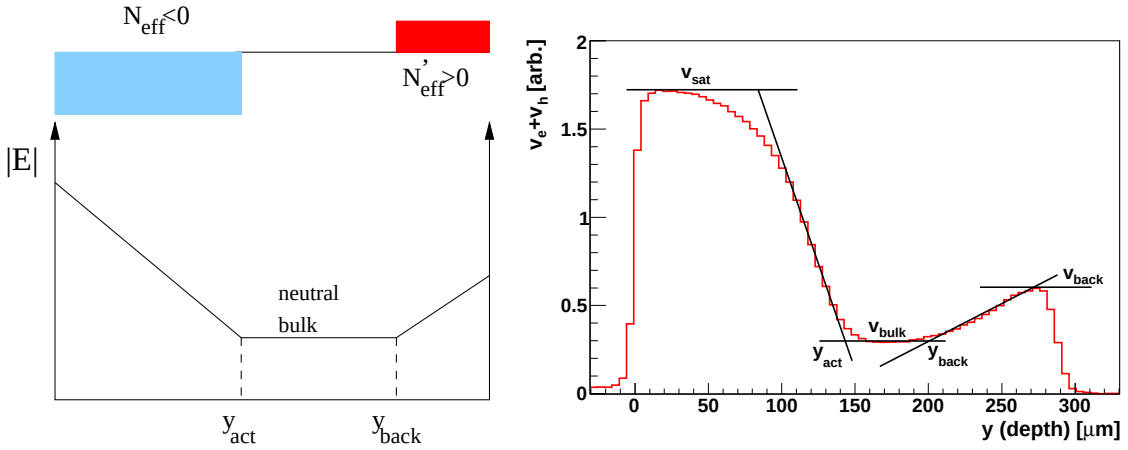

Figure 5. (a) The effective space charge and electric field model used in the work. (b) An example of determination of basic parameters from the measured velocity profile after receiving $2 \cdot 10^{15}\,\mathrm{cm}^{-2}$, annealed for 80 min at 60°C and biased to 500 V.

highest fluences expected at HL-LHC. One should however note that velocity saturates with electric field, therefore the second peak corresponds to significantly smaller electric field (see next sections).

In principle it should be straightforward to extract the electric field profile from the velocity profile by using $v_e + v_h = \left[\mu_e(E) + \mu_h(E)\right] E$. However at high electric fields the signal becomes insensitive to changes in the electric field due to drift velocity saturation. In addition the measured drift velocity profile is an average over the strip width. Any lateral dependence of the field which inevitably occurs close to the strips prevents a straightforward extraction of the field. However, the shape of the velocity profiles allows for modeling of the field with a small number of free parameters.

4 Field modeling in neutron irradiated detector

Introduction of acceptors upon irradiation creates negative space charge in the active region of the detector volume. This was confirmed by many measurements at lower fluences. However the velocity profiles as shown in figure 4 can occur only if the space charge changes sign inside the detector; i.e. it is negative on one side and positive on the other side. A schematic view of the simple model explaining the gross shape of the velocity profile can be seen in figure 5a. The basic reason for the two space charge regions (SCR) is the diffusion of carriers from the highly doped regions into the poorly doped bulk, assisted by flushing out the free carriers by the electric field in the front, reverse biased n^+p junction. The SCR at the backside pp^+ junction balances out diffusion and field currents. Trapping of the increasing concentration of electrons or holes from the generation current in the front SCR towards each end can modify the electric field [23–25].

In the simplest case, N_{eff} could be assumed constant in both SCR's (see figure 5a). Such a space charge leads to linear dependence of electric field at both detector ends and constant field in the so called electrically neutral bulk (ENB). This is commonly assigned zero value, but an electric field is needed at least to transport the carriers generated in the front SCR across the ENB. Although such an abrupt junction approximation is not entirely realistic, the model may still serve

2014 JINST 9 P10016

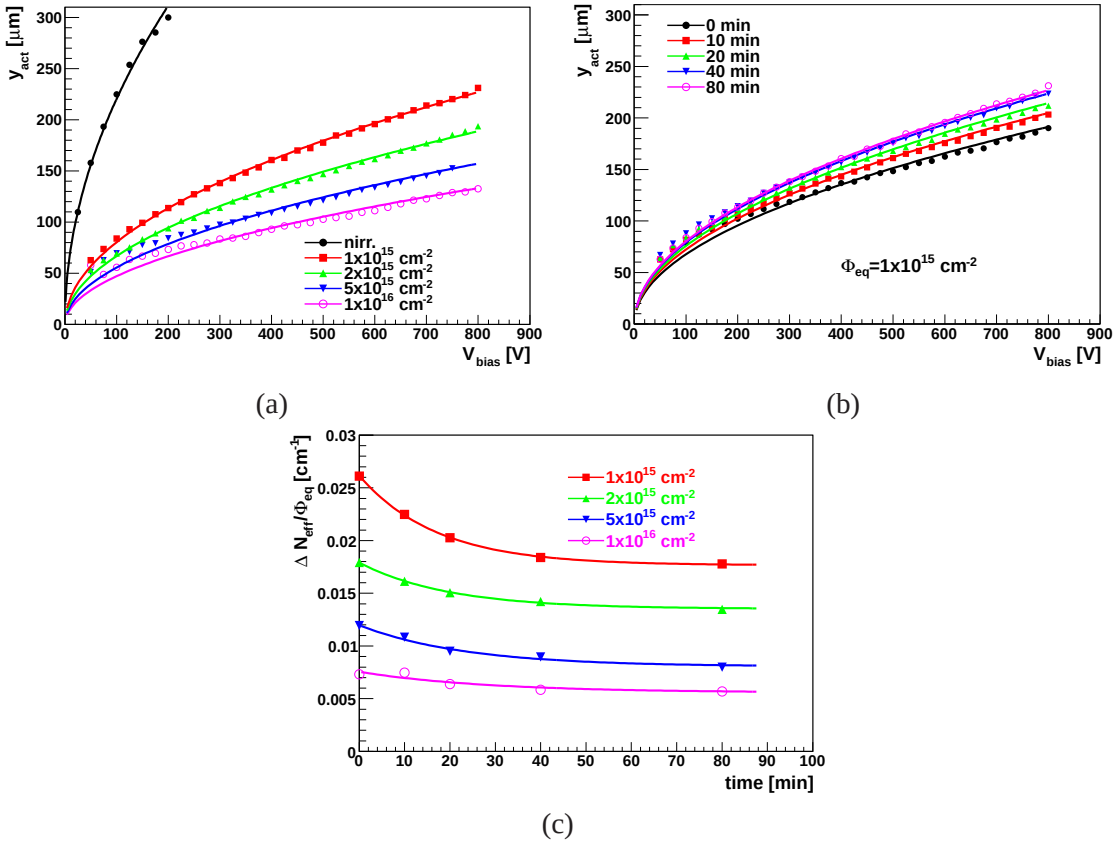

Figure 6. (a) Dependence of y_{act} on voltage for different fluences (annealed for 80 min) (b) Dependence of y_{act} on annealing time for the irradiation fluence of $1 \cdot 10^{15}\,\mathrm{cm}^{-2}$. The fits of eq. (4.1) to the data are shown by solid lines. (c) $\Delta N_{\mathrm{eff}}/\Phi_{\mathrm{eq}}$ vs. annealing time for all fluence steps (finalized from [20]).

the purpose of adequate description of measured profiles, hence it was used in the rest of the paper. Moreover, the observed dependence on voltage, especially of the front $\mathrm{n}^{+}\mathrm{p}$ junction, allows the conclusion that constant N_{eff} is indeed a viable approximation, particularly at lower fluences.

In general, one can look at the following parameters: widths of both SCR's y_{act}, $W - y_{\mathrm{back}}$, ratio of drift and saturation velocity in the bulk and at the back $v_{\mathrm{bulk}}/v_{\mathrm{sat}}$, $v_{\mathrm{back}}/v_{\mathrm{sat}}$ as a basic set that has to be matched by any model shape of $N_{\mathrm{eff}}(y)$. An example of extraction of these parameters from the velocity profiles is shown in figure 5b. The drift velocity close to strips at the highest voltages is defined as saturation velocity v_{sat}. A linear fit to the velocity profile is made on both sides of the SCR's facing the ENB. Their intersection with constant velocity v_{bulk} in ENB determines y_{act} and y_{back} as well as $v_{\mathrm{bulk}}/v_{\mathrm{sat}}$. The velocity at the back side of the detector is used to calculate $v_{\mathrm{back}}/v_{\mathrm{sat}}$.

4.1 Active region — junction side

The dependence of the junction region width, y_{act}, on voltage is shown for all fluences after 80 min annealing in figure 6a. If constant N_{eff} is assumed and voltage drop in ENB and at the back side of detector can be neglected then y_{act} should scale as

$$y_{\mathrm{act}} = \sqrt{\frac{2\,\varepsilon_{Si}\,V_{\mathrm{bias}}}{e_0\,N_{\mathrm{eff}}}}\,. \tag{4.1}$$

2014 JINST 9 P10016

Table 1. The parameters obtained from the fit of eq. (4.2) to the data shown in figure 6c. The parameter g_{ba} obtained from the fit was scaled by the ratio of total fluence and the fluence received in the last step. The reference values are $g_c = 0.017 - 0.019\,\mathrm{cm}^{-1}$, $g_{ba} \approx 0.014 - 0.018\,\mathrm{cm}^{-1}$, $\tau_{ba} = 21$ min [2, 18] .

Φ_{eq} $[\mathrm{cm}^{-2}]$	g_c $[\mathrm{cm}^{-1}]$	g_{ba} $[\mathrm{cm}^{-1}]$	τ_{ba} [min]
$10^{15}\,\mathrm{cm}^{-2}$	0.0176	0.0085	17.2
$2\cdot10^{15}\,\mathrm{cm}^{-2}$	0.0135	0.0088	20.5
$5\cdot10^{15}\,\mathrm{cm}^{-2}$	0.0078	0.0067	26.25
$10^{16}\,\mathrm{cm}^{-2}$	0.0056	0.004	27.8

where e_0 is elementary charge and ε_{Si} absolute permittivity of Silicon. The fit of eq. (4.1) to the data with N_{eff} as free parameter reveals that the agreement is good for lower fluences, while at higher fluences y_{act} is somewhat larger at low voltages than given by the fit. The fact that y_{act} follows eq. (4.1) strengthens the assumption of constant N_{eff} in the front SCR.

Figure 6b shows y_{act} at different annealing times. The evolution follows the expected behavior in accordance with the Hamburg model [2]. Initial decrease of active acceptors results in increase of y_{act}. After around 80 min at 60°C short term annealing is completed. Increase of effective acceptors during long term annealing occurs on much longer time scale than that in our measurements and was neglected. This allows for determination of introduction rates of short term and stable damage from

$$\frac{\Delta N_{\mathrm{eff}}}{\Phi_{\mathrm{eq}}} = \frac{N_{\mathrm{eff}} - N_{\mathrm{eff},0}}{\Phi_{\mathrm{eq}}} \approx g_c + g_{ba}\exp(-t/\tau_{ba}), \tag{4.2}$$

where g_c denotes the introduction rates of defects stable in time, g_{ba} defects that anneal out with time constant τ_{ba} and $N_{\mathrm{eff},0}$ initial concentration of acceptors. The results are shown in figure 6c together with a fit of eq. (4.2) to the data. The parameters determined from the fit g_c, g_{ba}, and τ_{ba} are gathered in table 1. At larger fluences one should bear in mind that the detector was irradiated in several steps and only the part of the damage received in the last step undergoes short term annealing. Therefore the introduction rate of the defects undergoing short term annealing g_{ba} was scaled by the ratio of total fluence and fluence received in the last step to get true introduction rate of defects undergoing short term annealing.

Up to $2\cdot10^{15}\,\mathrm{cm}^{-2}$ the agreement with low fluence data [2, 18], obtained from C-V is satisfactory. This means that voltage drop in ENB and the back SCR is small compared to the drop at the front junction. At larger fluences the effective space charge concentration compatible with measured y_{act} is significantly smaller than extrapolated from low fluence measurements. In addition, significantly larger voltage drop at higher fluences in the ENB and the back SCR, if accounted for, would reduce this effective space charge even further. It is evident that at larger fluences not only is there a significant electric field at the back of the detector and in the bulk, but also the main junction penetrates much deeper in the detector bulk than predicted.

The annealing parameters listed in table 1 are in rough agreement with RD48 at all fluences. The somewhat larger discrepancy of g_{ba} could be due to non-accounting of annealing effects during the irradiations and annealing effects of the previous irradiation fractions. Also there might be a hint of decreasing g_{ba} value with fluence.

2014 JINST 9 P10016

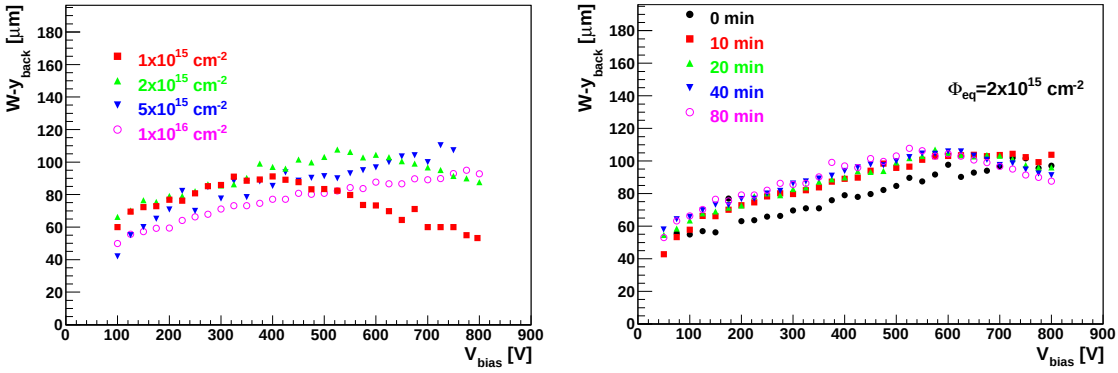

(a) (b)

Figure 7. Dependence of back SCR width $w - y_{\text{back}}$ on voltage for: (a) different fluences after 80 min annealing (b) different annealing times for a detector at accumulated fluence of $2 \cdot 10^{15}\,\text{cm}^{-2}$ (finalized from [20]).

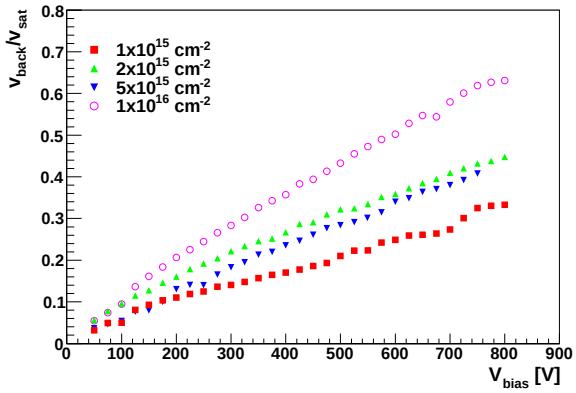

Figure 8. $v_{\text{back}}/v_{\text{sat}}$ vs. voltage plot at different fluences (finalized from [20]).

4.2 Electric field at the back electrode

The width of the SCR at the back of the detector, $W - y_{\text{back}}$, does not show significant dependence on fluence as can be seen in figure 7a. It grows with voltage almost linearly with a slope of $\sim 0.1\,\text{V}/\mu\text{m}$ up to the point where y_{act} approaches y_{back}. At higher voltages, y_{back} starts to increase again i.e. the back region shrinks, which can be seen for the detector after $\Phi_{\text{eq}} = 10^{15}\,\text{cm}^{-2}$ beyond 400 V. This effectively means that the ENB region disappeared, and the front SCR starts penetrating the back SCR.

There seems to be little dependence of $W - y_{\text{back}}$ on annealing as well (see figure 7b). The sample was irradiated to $\Phi_{\text{eq}} = 2 \cdot 10^{15}\,\text{cm}^{-2}$ and only after the last annealing step one can observe joining of the regions with opposite sign of the space charge; i.e. increase of y_{back} for voltages above 600 V.

The drift velocity at the back of the detector increases almost linearly with applied bias voltage as shown in figure 8. In all cases the bias voltage applied was lower than V_{fd}. As it can be seen $v_{\text{back}}/v_{\text{sat}} \approx 0.45$ after fluence of $\Phi_{\text{eq}} = 2 \cdot 10^{15}\,\text{cm}^{-2}$ at 800 V, which corresponds to electric field $\sim 0.5\,\text{V}/\mu\text{m}$.

2014 JINST 9 P10016

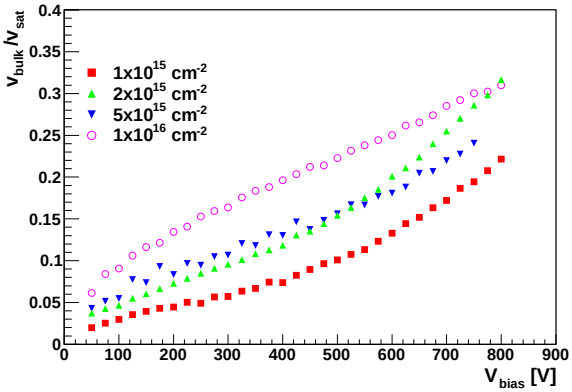

Figure 9. Dependence of drift velocity in the neutral bulk on voltage for different fluences (finalized from [20]).

4.3 Neutral bulk

The drift velocity in the ENB is shown for all fluences and voltages investigated in figure 9. As can be seen the velocity increases with fluence and voltage. The velocity in the bulk reaches around one third of the saturated one. This translates to electric field strength of around 0.3 V/μm. This is in agreement with observations made in ref. [23]. Such a substantial electric field effectively implies that at high fluences the whole detector is active already at low bias voltages.

5 Pion and mixed irradiated detectors

Two detectors were irradiated with 200 MeV pions at Paul Scherrer Institute in Villingen, Switzerland [26]. Although typical energy of pions at the LHC is few GeV [3], identical effects of 200 MeV pion and 23 GeV proton irradiations to the detector operation, which are also consistent with displacement damage function [27], indicate that the type of damage caused by 200 MeV pions is similar to that of few GeV ones.

Due to the availability of the facility only moderate equivalent fluences of $\Phi_{eq} = 4.6 \cdot 10^{14}$ cm^{-2} and $\Phi_{eq} = 1.6 \cdot 10^{15}$ cm^{-2} were reached. The hardness factor 1.14 was used to convert pion fluence to the equivalent fluence of 1 MeV neutrons. The fluences are accurate to 8% [28].

The velocity profiles in pion irradiated detectors are shown in figure 10. The difference between pion and neutron irradiated detectors is striking. For the lower fluence a high electric field is present in the whole detector volume already at ≈ 200 V. This means that after receiving $\Phi_{eq} = 4.6 \cdot 10^{14}$ cm^{-2} the voltage required to establish the field in the entire detector is almost identical to the one before irradiation. Although there was no deliberate oxygenation of the wafers the concentration of the oxygen was rather high $[O] > 10^{17}$ cm^{-3} [29]. Oxygen is known to give rise to the introduction of positive space charge after charged hadron irradiations [30]. Usually the introduction of negative space charge nevertheless prevails, but for this particular material traps, responsible for positive and negative space charge seem to have been introduced with approximately same rates. The shape of the velocity profile at low voltages indicates that the main junction remains at the strip side. Even more interesting are velocity/electric field profiles at the high pion fluence of $\Phi_{eq} = 1.6 \cdot 10^{15}$ cm^{-2}, which are almost symmetrical with respect to both contacts. Only around

2014 JINST 9 P10016

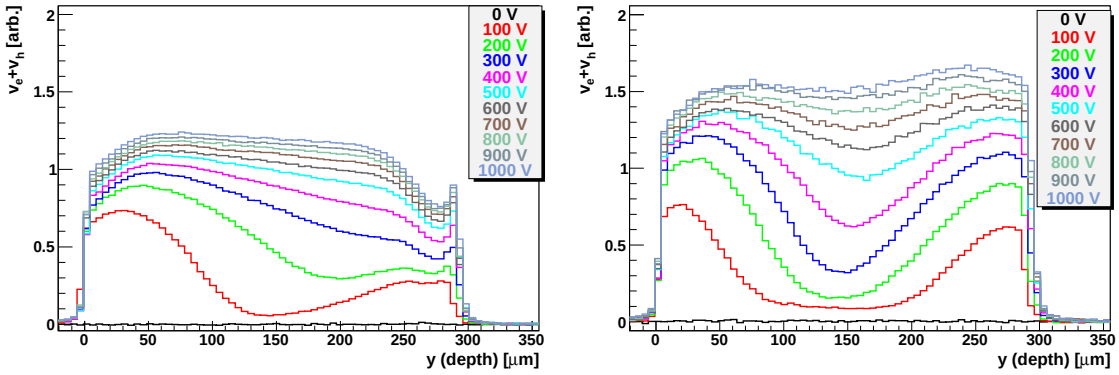

(a) (b)

Figure 10. Velocity profiles of samples irradiated with pions to (a) $\Phi_{\text{eq}} = 4.6 \cdot 10^{14}\,\text{cm}^{-2}$ and (b) $\Phi_{\text{eq}} = 1.6 \cdot 10^{15}\,\text{cm}^{-2}$.

200 V is required for substantial electric field in the whole detector volume and around 500 V to achieve high drift velocity in a major part of the detector volume. Such a beneficial velocity profile is reflected in very good charge collection of > 12000 e at 500 V as reported in ref. [29].

For the detector irradiated to the lower fluence the model parameters could be reliably determined only for lowest voltages. Already at 200 V it becomes difficult to identify the regions. At the higher fluence y_{act} and $W - y_{\text{back}}$ merge in the middle of the detector already at < 200 V with velocities at both ends almost identical. Although the model parameters could in principle be extracted the information gained would be limited to the simple explanation above.

At the LHC experiments detectors are exposed to a mixture of fast charged hadrons and neutrons, with their ratio depending on the distance from the interaction point. Neutrons produce predominately cluster defects while charged hadrons produce a large fraction of point defects. The manifestation of the damage is therefore different for neutrons and charged hadrons. In order to see the effects of both irradiation particle types (mixed irradiations) both pion-irradiated samples were irradiated also with neutrons.

Introduction of negative space charge after additional neutron irradiation, shown in figure 11, alters the velocity profiles in an expected way with larger velocity at the strip side as a consequence of additional introduction of negative space charge. One should note that while the pion and neutron fluences were comparable for the lower fluence, the pion fluence exceeds the neutron fluence by 60% in the higher mixed fluence sample. A comparison of figure 4a and 11a where equivalent fluences are similar, shows a more uniform profile for the mixed irradiated sample. This can be seen even more clearly for the sample irradiated to $\Phi_{\text{eq}} = 2.6 \cdot 10^{15}\,\text{cm}^{-2}$ shown in figure 11b, which differs significantly from the neutron-only irradiated sample at $\Phi_{\text{eq}} = 2 \cdot 10^{15}\,\text{cm}^{-2}$ (see figure 4b). For the former, the drift velocity is substantial in larger part of the detector than for the latter. Although the velocity profile looks relatively symmetric the electric field profile is much less symmetric, due to saturation of the velocity at high electric fields. The difference between the drift velocities at the back and front is only about a factor of 1.7 at 500 V, but this corresponds to a factor of four in the electric field strength. Even at 1000 V where the drift velocity in the whole bulk appears comparable the electric field is still strongest at the strips.

2014 JINST 9 P10016

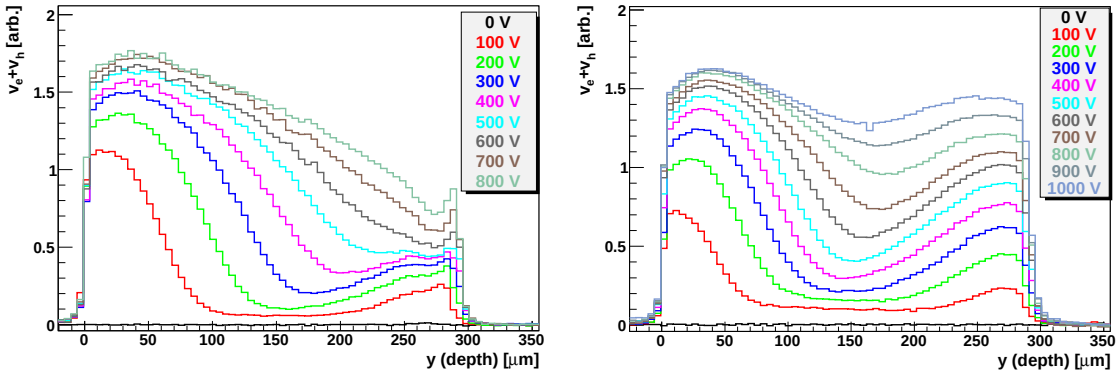

(a) (b)

Figure 11. Velocity profiles of samples irradiated with pions and neutrons for: (a) same detector as in figure 10a, after additional neutron fluence of $\Phi_{eq} = 5 \cdot 10^{14}\,\mathrm{cm}^{-2}$, (b) same detector as in figure 10b after additional neutron fluence of $\Phi_{eq} = 1 \cdot 10^{15}\,\mathrm{cm}^{-2}$.

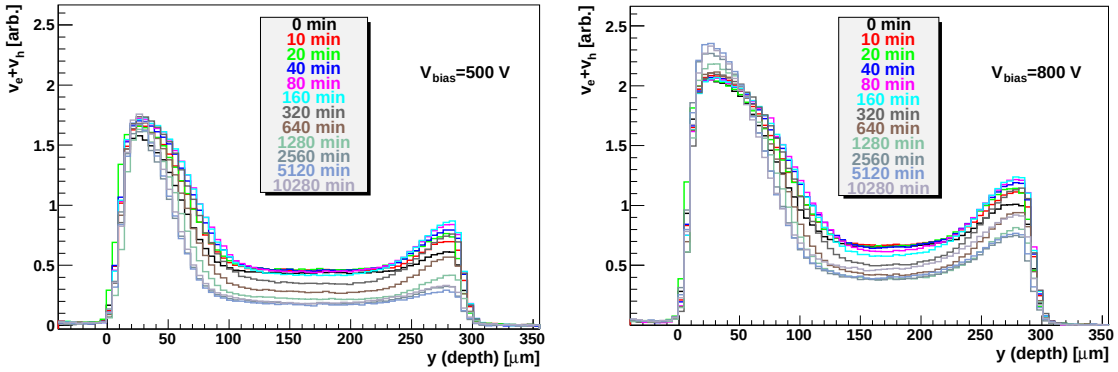

(a) (b)

Figure 12. Velocity profiles of samples irradiated with neutrons to $\Phi_{eq} = 1 \cdot 10^{16}\,\mathrm{cm}^{-2}$ (a) 500 V and (b) 800 V after different annealing steps.

6 Long term annealing

After the last irradiation step the neutron irradiated sample underwent long term annealing at 60°C. The velocity profiles taken during annealing are shown in figure 12 for two different bias voltages. At 500 V y_{act} decreases with annealing so do the v_{bulk} and v_{back}. This in turn leads to the increase of electric field near the strips, which however can not be observed in the velocity profile due to saturation of the drift velocity. The field is still too low to observe increase of charge collection due to impact multiplication and the collected charge $\left(1/W \int_0^W Q(y)dy\right)$ decreases with annealing time [31].

At larger bias voltages the charge multiplication changes the velocity profiles close to the strips. After long annealing times $v_h + v_e$ increases beyond the saturation velocity, which is a clear indication of charge multiplication (increase of $N_{e,h}$ in eq. (3.1)). This leads to a significant increase of charge collection [31], but the model parameters (v_{bulk}, v_{back}, y_{act}) show the same behavior as at lower voltages. The dependence of model parameter y_{act} on annealing times is shown in figure 13.

2014 JINST 9 P10016

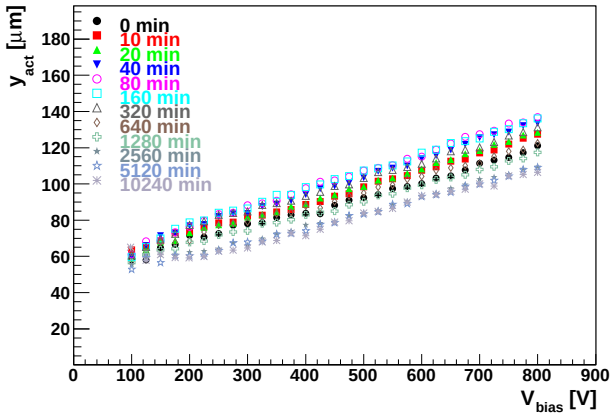

Figure 13. Evolution of active region of the detector irradiated to $\Phi_{\mathrm{eq}} = 1 \cdot 10^{16}\,\mathrm{cm}^{-2}$ at different annealing times.

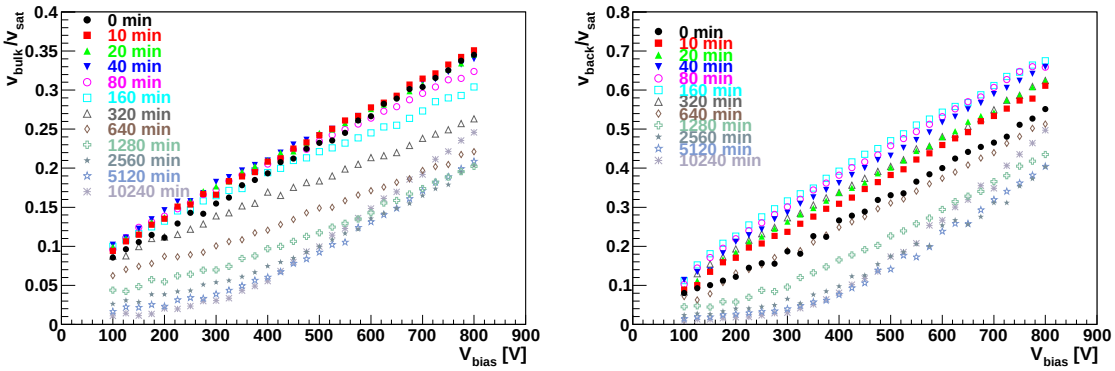

(a) (b)

Figure 14. Dependence of (a) v_{bulk} and (b) v_{back} on voltage for the different annealing times of the detector irradiated to $\Phi_{\mathrm{eq}} = 1 \cdot 10^{16}\,\mathrm{cm}^{-2}$.

The decrease of the active region with annealing times is significant and can be explained by activation of effective acceptors during annealing, which on one side reduce the y_{act}, but also give rise to charge multiplication due to impact ionization. An active region of 50 μm at already 100 V was observed. Comparison of $y_{\mathrm{act}}(V)$ after $t_1 = 80$ min and $t_2 = 10240$ min annealing allows for a rough estimation of effective acceptors concentration ratio, providing that constant N_{eff} is assumed. It follows from the eq. (4.1) that $y_{\mathrm{act}}(V_{\mathrm{bias}}, t_1)/y_{\mathrm{act}}(V_{\mathrm{bias}}, t_2) = \sqrt{N_{\mathrm{eff},2}/N_{\mathrm{eff},1}} \sim 2$, which points to comparable introduction rates of stable acceptors and acceptors activated during long term annealing. Even for an oxygen rich detector the latter is lower than found at lower fluences [2].

It can be seen in figure 14 that at lower voltages and large annealing times the voltage drop occurs almost entirely in the active region as the v_{bulk} and v_{back} vanish and start to rise with approximately the same slope as for shorter annealing times only after ~ 400 V. Around 500 V is required after the last annealing step to have the same $v_{\mathrm{bulk}}/v_{\mathrm{sat}}$ and $v_{\mathrm{back}}/v_{\mathrm{sat}}$ as before the long term annealing at 100 V.

2014 JINST 9 P10016

7 Simulation of the Edge-TCT measurements

Measured velocity profiles were simulated by assuming constant space charge in both regions, active and back as shown in figure 5a. The model parameters as determined from the measurements and shown in previous sections were fed back to the simulation to check if the measured velocity profiles can be reproduced with adequate accuracy.

The details of the simulation can be found in refs. [32–34]. The calculation of electric field and weighting field in the investigated detector is based on numerical solution of Poisson and Laplace equations on a mesh of $0.5 \times 0.5\,\mu\text{m}^2$ for the corresponding potentials. A segment of 7 strips ($700 \times 300\,\mu\text{m}^2$) was simulated. The simulator took $N_{\text{eff}}(x,y)$ as an input and did not derive it from the defects' properties.

The drift of the generated carriers was done in steps by numerically solving drift equation ($d\vec{r} = \vec{v}(\vec{r}(t))\,dt$). The contribution to the induced current was calculated for each step according to eq. (3.1). Although the simulation included impact ionization, it should however be noted that the simulated gain is unreliable for two reasons: the unknown shape of the implant which plays a role in focusing of field lines and, more importantly, the holes released in the multiplication get trapped and moderate the field. In the model of constant N_{eff} this was not not taken into account leading to large discrepancies between simulations and measurements.

An example of the drift paths of the free carriers generated by a Gaussian beam of infrared light ($\lambda = 1064\,\mu\text{m}$) is shown in figure 15a. The resulting induced currents were fed to the simulation of a simple *RC* circuitry with ($C_{\text{strip}} \sim 2\,\text{pF}$, $R_{\text{amp}} = 50\,\Omega$, $RC = 100\,\text{ps}$) to account for electronics transfer function in the measurements. In the figure 15b the measured and simulated induced currents are shown for the non-irradiated detector. Although the duration of the pulse was not perfectly reproduced the initial part of the current pulse was. The average response in initial 375 ps was taken as the measure of $v_e + v_h$. The measured rise time of the current pulse was slightly longer than simulated (calculated *RC*) therefore τ_{sample} used in measurements corresponds to shorter τ_{sample} in simulations, but as shown in figure 3 the difference has little or no impact on extracted $v_e + v_h$.

The resulting velocity profiles are shown in figure 15c at 200 V. A reasonable agreement is obtained in the most of the volume except near the strips, where the simulation predicts larger current than observed in the measurements, and at the back where the p^+ layer was not taken into account.

The reason for the former is likely in the required boundary conditions at the detector surface, which require that all the field lines stay in the sensor (reflective boundary conditions). According to the recent measurements [35] the detector surface can sometimes act as equipotential plane. If this boundary condition was used the bump in the velocity profile disappeared (implant width $\text{iw} = 100\,\mu\text{m}$), but the simulated drift velocity near the strips was too low due to the initial drift in the lower weighting field. The weighting field is determined by the width of Al electrodes ($20\,\mu\text{m}$). The velocity profile for an intermediate implant width $\text{iw} = 40\,\mu\text{m}$ lies in-between. Moreover, in case of reflective boundary conditions somewhat larger voltage is required for depletion than in the case of equipotential plane for the same $N_{\text{eff}}(y)$. It can therefore be concluded that the choice of the boundary condition and properties of the detector surface affects the simulation results.

The effective trapping times at large fluences were taken from ref. [36]. It was shown in this reference that effective trapping times at large fluences may be longer than those extrapolated from lower fluences [16]. The comparison of measured and simulated velocity profiles using reflective

2014 JINST 9 P10016

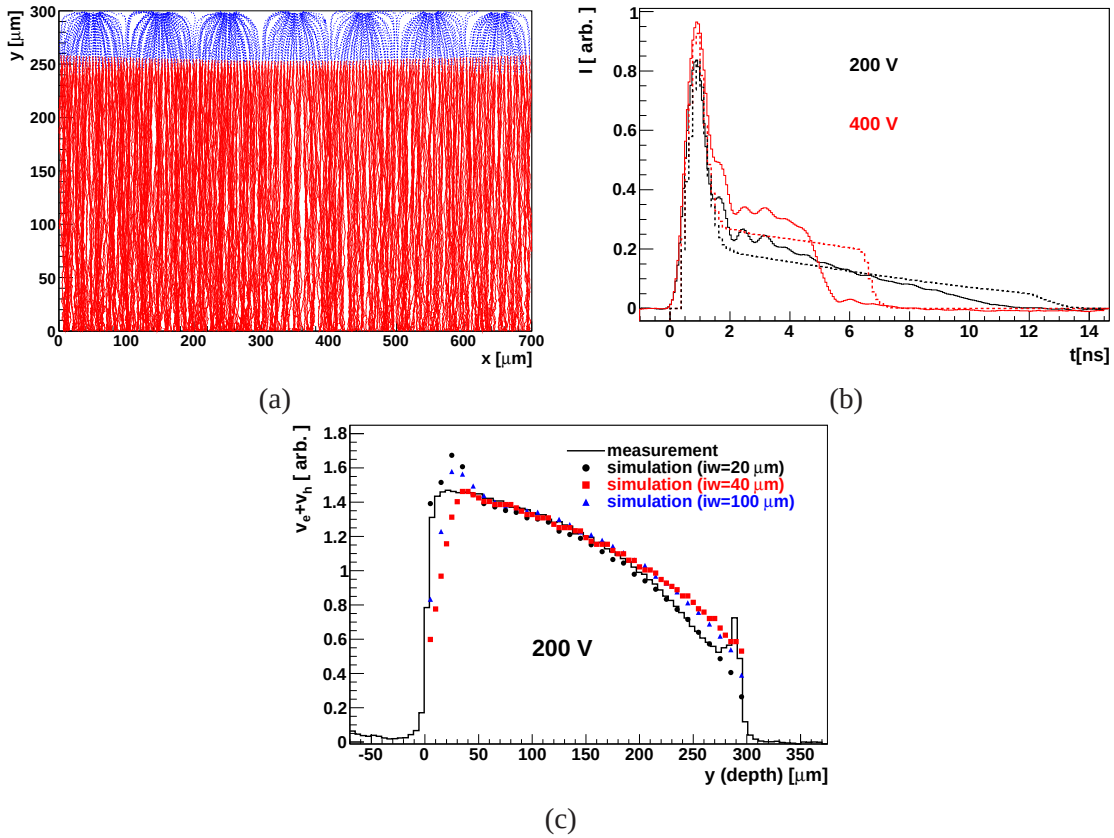

Figure 15. (a) Example of simulated drift paths of electrons (blue) and holes (red) created by a Gaussian beam 50 μm away from the strips ($V_{\text{bias}} = 200$ V). Note that the strips are at $y = 300\,\mu$m. (b) Simulated (dashed line) and measured (solid line) induced currents for the beam 50 μm away from the strips. (c) Measured and simulated velocity profiles for different widths of the implant (iw) used to calculate electric field.

boundary condition is shown in figure 16. The agreement at lower fluences is adequate, although for $y < y_{\text{act}}$ simulated velocity profile gives larger values than measured, which means that the electric field away from the strips is smaller than given by the assumption of a constant space charge. For the lower two fluences and investigated bias voltage range the electric fields were low enough for impact ionization not to affect the velocity profiles.

Although the space charge concentration at the back ($y > y_{\text{back}}$) was spatially constant, it had to depend on voltage in order to reproduce the measurements. The dependence was found approximately linear $N'_{\text{eff}} = N'_{\text{eff},0} + k_{\text{back}} \cdot V_{\text{bias}}$ with $N'_{\text{eff},0} = 0.23 \cdot 10^{12}\,\text{cm}^{-3}$, $k_{\text{back}} = 1.25 \cdot 10^{9}\,\text{cm}^{-3}\,\text{V}^{-1}$ for the $\Phi_{\text{eq}} = 10^{15}\,\text{cm}^{-2}$ and $N'_{\text{eff},0} = 0.5 \cdot 10^{12}\,\text{cm}^{-3}$, $k_{\text{back}} = 1.9 \cdot 10^{9}\,\text{cm}^{-3}\,\text{V}^{-1}$ for the $\Phi_{\text{eq}} = 2 \cdot 10^{15}\,\text{cm}^{-2}$.

At high bias voltages and larger fluences ($\Phi_{\text{eq}} = 5 \cdot 10^{15}\,\text{cm}^{-2}$ and $\Phi_{\text{eq}} = 10^{16}\,\text{cm}^{-2}$) the impact ionization had to be taken into account. However, a model with voltage independent spatially constant N_{eff} failed at high voltages where charge gain becomes large. As already mentioned moderation of the field by reducing the negative space charge through trapped holes produced in impact ionization was not considered, hence simulated induced currents near the strips showed unrealistically high values.

2014 JINST 9 P10016

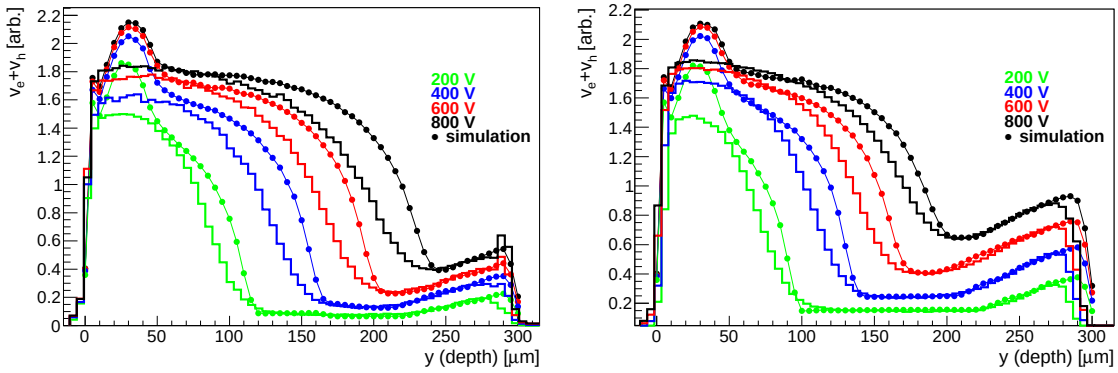

Figure 16. Comparison of measured and simulated velocity profiles of irradiated detectors (a) $\Phi_{eq} = 10^{15}\,\mathrm{cm}^{-2}$ and (b) $\Phi_{eq} = 2 \cdot 10^{15}\,\mathrm{cm}^{-2}$. Note that all input parameters, but N'_{eff}, were extracted from measurements shown in previous sections, e.g. for the detector at 400 V and irradiated to $\Phi_{eq} = 10^{15}\,\mathrm{cm}^{-2}$, $N_{eff} = 1.76 \cdot 10^{13}\,\mathrm{cm}^{-3}$, $y_{act} = 160\ \mu$m, $W - y_{back} = 90\ \mu$m.

8 Conclusions

A silicon micro-strip n-on-p type sensor was irradiated with neutrons to fluences up to $\Phi_{eq} = 1 \cdot 10^{16}\,\mathrm{cm}^{-2}$. Edge-TCT was used to extract the velocity profiles. The velocity profiles reveal the existence of two SCR's with opposite sign of space charge and ENB in-between. The electric field was parameterized by a simple model assuming constant effective space charge at the junction and at the back electrode. The borders of both SCR's, velocity in the ENB and at the back electrode were determined as a function of fluence and voltage. It was shown that the assumption of constant N_{eff} increasing with fluence describes the evolution of the SCR at the junction, with the introduction rates of effective acceptors showing saturation effects at the high fluence end.

The pion irradiated detectors exhibit more uniform and symmetric velocity profiles, probably because of high oxygen concentration and related deep active donor generation. Additional acceptors introduced through neutron irradiation change the velocity profile in the expected way — increase of electric field at the main junction, but still with more homogeneous velocity profile than the detector irradiated to approximately the same fluence exclusively with neutrons.

The long term annealing studies of the neutron irradiated detector to $\Phi_{eq} = 10^{16}\,\mathrm{cm}^{-2}$ showed that the active region decreases with time as well v_{bulk} and v_{back}. This in turn means larger electric field close to the strips which leads to increased charge multiplication.

The measured model parameters were fed to a device simulator. The agreement between simulation and measurements is adequate, but the model of voltage independent spatially constant effective doping concentration for $y < y_{act}$ fails at high fluences. Most probable reason is the absence of field moderation through trapped holes produced close to the strips by the impact ionization.

The model parameters extracted from the measurements serve as anchor points for any modeling or calculation of the electric field in the irradiated silicon detectors. The same set of parameters should be established also for the detectors irradiated by fast charged hadrons, along with their dependence on the silicon material and during the long term annealing at different fluences.

2014 JINST 9 P10016

References

[1] F. Gianotti et al., *Physics potential and experimental challenges of the LHC luminosity upgrade*, *Eur. Phys. J.* **C 39** (2005) 293 [hep-ph/0204087].

[2] ROSE collaboration, G. Lindström et al., *Radiation hard silicon detectors — developments by the RD48 (ROSE) Collaboration*, *Nucl. Instrum. Meth.* **A 466** (2001) 308.

[3] I. Dawson, *Radiation background simulation and verification at the LHC: Examples from the ATLAS experiment and its upgrades*, PoS(Vertex 2012)015.

[4] C. Da Via and S.J. Watts, *Can silicon operate beyond* 10^{15} *neutrons* cm^{-2}*?*, *Nucl. Instrum. Meth.* **A 501** (2003) 138.

[5] C. Da Via et al., 3*D silicon sensors: Design, large area production and quality assurance for the ATLAS IBL pixel detector upgrade*, *Nucl. Instrum. Meth.* **A 694** (2012) 321.

[6] J. Weingarten et al., *Planar Pixel Sensors for the ATLAS Upgrade: Beam Tests results*, 2012 *JINST* **7** P10028 [arXiv:1204.1266].

[7] G. Casse, A. Affolder, P.P. Allport, H. Brown and M. Wormald, *Enhanced efficiency of segmented silicon detectors of different thicknesses after proton irradiations up to* $1 \times 10^{16} n_{\mathrm{eq}}\,\mathrm{cm}^2$, *Nucl. Instrum. Meth.* **A 624** (2010) 401.

[8] RD50 collaboration, F. Hartmann, *Recent advances in the development of semiconductor detectors for very high luminosity colliders*, *Nucl. Instrum. Meth.* **A 617** (2010) 543.

[9] C.A. Lee et al., *Ionization rates of holes and electrons in Si*, *Phys. Rev.* **134** (1964) A761.

[10] R. Van Oversraeten and H. De Man, *Measurement of the ionization rates in diffused silicon p-n junctions*, *Solid State Electron.* **13** (1970) 583.

[11] I. Mandic, V. Cindro, G. Kramberger and M. Mikus, *Measurement of anomalously high charge collection efficiency in* n^+p *strip detectors irradiated by up to* $10^{16}\,n_{\mathrm{eq}}/\mathrm{cm}^2$, *Nucl. Instrum. Meth.* **A 603** (2009) 263.

[12] G. Casse et al., *Can we claim charge multiplication in heavily irradiated segmented detectors?*, presented at *14th RD50 Workshop*, Freiburg, Germany, 5–7 June 2009.

[13] M. Petasecca, F. Moscatelli, D. Passeri, G.U. Pignatel and S. Scarpello, *Numerical simulation of radiation damage effects in p-type silicon detectors*, *Nucl. Instrum. Meth.* **A 563** (2006) 192.

[14] V. Eremin, E. Verbitskaya and Z. Li, *The origin of double peak electric field distribution in heavily irradiated silicon detectors*, *Nucl. Instrum. Meth.* **A 476** (2002) 556.

[15] V. Eremin, N. Strokan, E. Verbitskaya and Z. Li, *Development of transient current and charge techniques for the measurement of effective net concentration of ionized charges (N(eff in the space charge region of p-n junction detectors*, *Nucl. Instrum. Meth.* **A 372** (1996) 388.

[16] G. Kramberger, V. Cindro, I. Mandic, M. Mikuz and M. Zavrtanik, *Effective trapping time of electrons and holes in different silicon materials irradiated with neutrons, protons and pions*, *Nucl. Instrum. Meth.* **A 481** (2002) 297.

[17] RD50 collaboration, O. Krasel et al., *Measurement of trapping time constants in proton-irradiated silicon pad detectors*, *IEEE Trans. Nucl. Sci.* **51** (2004) 3055.

[18] V. Cindro et al., *Radiation damage in p-type silicon irradiated with neutrons and protons*, *Nucl. Instrum. Meth.* **A 599** (2009) 60.

2014 JINST 9 P10016

[19] G. Kramberger et al., *Investigation of Irradiated Silicon Detectors by Edge-TCT*, *IEEE Trans. Nucl. Sci.* **57** (2010) 2294.

[20] RD50 collaboration, G. Kramberger et al., *Electric field modeling in heavily irradiated silicon detectors based on edge TCT measurements*, PoS(Vertex 2012)022.

[21] L. Snoj, G. Žerovnik and A. Trkov, *Computational analysis of irradiation facilities at the JSI TRIGA reactor*, *Appl. Radiat. Isot.* **70** (2012) 483.

[22] D. Zontar, V. Cindro, G. Kramberger and M. Mikuz, *Time development and flux dependence of neutron-irradiation induced defects in silicon pad detectors*, *Nucl. Instrum. Meth.* **A 426** (1999) 51.

[23] I. Mandic, V. Cindro, G. Kramberger, M. Mikuz and M. Zavrtanik, *Charge-collection efficiency of heavily irradiated silicon diodes operated with an increased free-carrier concentration and under forward bias*, *Nucl. Instrum. Meth.* **A 533** (2004) 442.

[24] V. Eremin, Z. Li and I. Ilyashenko, *Trapping induced $N_{\rm eff}$ and electrical field transformation at different temperatures in neutron irradiated high resistivity silicon detectors*, *Nucl. Instrum. Meth.* **A 360** (1995) 458.

[25] D. Menichelli, M. Bruzzi, Z. Li and V. Eremin, *Modelling of observed double-junction effect*, *Nucl. Instr. and Meth.* **A 426** (1999) 135.

[26] User guide to accelerator facilities, Paul Scherrer Institute, Villigen and Wurenlingen, 2^{nd} edition, July 1994.

[27] M. Huhtinen and P.A. Aarnio, *Pion induced displacement damage in silicon devices*, *Nucl. Instrum. Meth.* **A 335** (1993) 580.

[28] M. Glaser, F. Ravotti and M. Moll, *Dosimetry assessments in the irradiation facilities at the CERN-PS accelerator*, *IEEE Trans. Nucl. Sci.* **53** (2006) 2016.

[29] RD50 collaboration, I. Mandic et al., *Accelerated annealing of n^+-p strip detectors irradiated with pions*, 2011 *JINST* **6** P11008.

[30] I. Pintiliea, G. Lindstroem, A. Junkes and E. Fretwurst, *Radiation Induced Point and Cluster-Related Defects with Strong Impact to Damage Properties of Silicon Detectors*, *Nucl. Instrum. Meth.* **A 611** (2009) 52 [arXiv:0907.3050].

[31] M. Milovanovič et al., *Effects of accelerated long term annealing in highly irradiated n^+-p strip detector examined by Edge-TCT*, 2012 *JINST* **7** P06007.

[32] G. Kramberger, *Signal formation in irradiated silicon detectors*, Ph.D. Thesis, University of Ljubljana, (2001) [CERN-THESIS-2001-038].

[33] G. Kramberger, V. Cindro and M. Mikuž, *Signals in non-irradiated and irradiated single-sided silicon detectors*, *Nucl. Instrum. Meth.* **A 457** (2001) 550.

[34] G. Kramberger and D. Contarato, *Simulation of signal in irradiated silicon pixel detectors*, *Nucl. Instrum. Meth.* **A 511** (2003) 82.

[35] R. Klanner et al., *Impact of low-dose electron irradiation on the charge collection of n^+-p silicon strip sensors*, presented at *Technology and Instrumentation in Particle Physics (TIPP14)*, Amsterdam, Netherlands, 2–6 June 2014, to appear in PoS.

[36] T. Poehlsen et al., *Trapping in p-on-n silicon sensors at fluences relevant for the HL-LHC*, presented at *24^{th} RD50 Workshop*, Bucharest, Romania, 11–13 June 2014.

2014 JINST 9 P10016